Sensors & Transducers, Vol. 262, Issue 3, September 2023, pp. 13-22

www.sensorsportal.com

Sensors & Transducers

Published by IFSA Publishing, S. L., 2023
http://www.sensorsportal.com

Automatic Brain Tumor Detection and Segmentation using Enhanced Optical Scanning Holography and Active Contour Model in MRI

[1, *]Anass CHERKAOUI, [1] Abdennacer EL-OUARZADI, [2] Abdelaziz ESSADIKE and [1] Abdenbi BOUZID

[1] Moulay Ismail University, Faculty of Sciences, Department of physics,
B.P. 11201 Zitoune Meknes, Morocco
[2] Hassan 1st University Faculty of Science and Technology, Higher Institute of Health Sciences,
BP : 577, Route de Casa, Settat, Morocco
[1] Tel. : 05-35-53-73-21 / 05-35-53-88-70, fax : 05-35-53-68-08 / 05 35 45 43 01
E-mail: an.cherkaoui@edu.umi.ac.ma

Received: 27 July 2023 Accepted: 30 August 2023 Published: 30 September 2023

Abstract: This paper aims to develop a fully automatic Magnetic Resonance Imaging Brain tumor segmentation and detection to tackle the problem of manual segmentation, which is an error-prone, sensitive, and time-absorbing process. We enhance our previous framework [1] for optical scanning holography to detect abnormal tissue regions in Magnetic Resonance Imaging in terms of acquisition speed, precision, and data size. The proposed method combines the in-line holography setup, performed by a heterodyne fringe pattern, and a Magnetic Resonance Imaging display assured by a spatial light modulator. The extraction of the maximum peaks In-phase component of the scanned current gives a reliable precision to the tumor's position. Simultaneously, this position is applied in an Active Contour Model to perform a fast segmentation of the region corresponding to the tumors. Various images of brain tumors from the BRATS database, which have different contrast and shape, are used to test the proposed method. The suggested method achieves high accurate detection of tumor tissue by returned parameters (L,c) by the Generalized Optical Scanning Holography method. In addition, compared to active contour-based methods, the proposed method offers faster and more reliable performance with very short average computation time per image.

Keywords: Optical scanning holography, Brain tumor detection, Active contour, Segmentation, In-phase component.

1. Introduction

Optical biomedical imaging has emerged these last years as an important area of research and development in diagnostic medicine driven by the need for safe, affordable, non-invasive modalities to detect and diagnose cellular abnormalities in the human body. The optical image processing field has undergone tremendous development and has found various applications ranging from optical image encryption [2], ophthalmological cancer detection [3], brain tumor detection and Magnetic Resonance Imaging (MRI), image segmentation [4], to biometric applications [5]. Its high-speed parallel processing makes it promising for the next generation of image processing techniques, replacing traditional numerical algorithms. There are four main aspects of optical image processing systems tackled; image pre-processing techniques to filter out noise and extracting specific regions of interest through new segmentation techniques, object feature extraction and detection techniques for locating areas of interest or altering

scene conditions, image processing applications that create intelligent instrumentation systems, and image encryption techniques to ensure security and safety of data communication [6].

The segmentation is the final process after having images of the biological agent through medical imaging modalities as optical imaging, radionuclide imaging, and MRI. For example, optical imaging is a scattering light-based technique. In this type of technique, the base methods can be classified into two modalities; one is a direct observation of the light rays passing through the structure tissue, and the other uses fluorescent contrast agents [7]. In addition, the new automatic segmentation methods for identifying and measuring volumetric structures with magnetic resonance imaging (MRI) [8, 9], Computed Tomography (CT) dose optimization [10], automatic reconstruction and segmentation for structural characterization of scanning electron microscopy images [11], and image-guided radiation therapy [12]. The proposed method solves the segmentation task in a way adapted to current needs, including in surface analysis like skin diseases [13], tumor localization in the human breast [14], eye diseases [15] and dosimetry planning in brain radiotherapy [16]. Radiotherapy aims to provide a curative and precise dose of radiation delivered to the target volume, i.e., the brain tumor, whilst sparing the surrounding risk organs. Given the problem's sensitivity, tumor segmentation is usually manually performed by neuroradiologists or using methods characterized by a lack of entirely automatic detection. The main disadvantage of these limitations directly affects the expected results in terms of accuracy and time-consuming.

Segmentation of the "brain" area of interest is a common preprocessing of MRI images. Unfortunately, this technique isolates the "brain" component from the initial data volume to limit the work areas during subsequent segmentation and thus improve the quality of the results obtained and reduce the computational complexity (in time and space) [3, 5, 15]. Recently, optical methods opened a new field to tackle this technological challenge due to the specificities of the constraints of different natures. This paper proposes a new architecture that extracts phase information corresponding to the tumor position by the enhanced optical scanning holography (OSH). Concurrently, an active contour model (ACM) is applied to this position to perform a faster segmentation of the region corresponding to the tumors in each slice. The underlying physics of this automatic extraction is driven by the In-phase component of the image scan current, which can also facilitate the calculation of the active contour energy terms and therefore alleviate the segmentation of the tumor tissue by rendering the segmentation as an energy minimization problem.

Optical scanning holography is a Realtime Holographic Recording technique wherein holographic information about a 3D three-dimensional object is collected using a single active optical scan in two dimensions. Implementations of this technique include optical scanning microscopy, 3D holographic display, pattern recognition, and optical remote sensing [17-20]. Following our previous work [1], we explored the use of OSH in automatizing tumor tissue detection in MRI. This paper proposes an enhanced framework for optical scanning holography (OSH) to detect abnormal tissue regions. The proposed method combines the in-line digital holography setup, a heterodyne fringe pattern, and an MR image display assured by a spatial light modulator (SLM). We improve [1] in terms of acquisition speed, accuracy, and data size. In addition, This technique the Generalized Optical Scanning Holography (GOSH) of recording holographic information is advantageous as two on-axis holograms are acquired simultaneously, unlike standard phase-shifting holography where their holograms are acquired sequentially. Hence, we can construct a complex hologram that does not create a double image in reconstruction from the two on-axis holograms [21-26].

2. Method

This section presents the scanning image process used, based on a typically two-pupil optical heterodyne. Since we consider that the automatic tumor detection is based on the In-phase component of the scanned current, we require to use a system to preserve this In-phase component throughout the data acquisition. From our investigation, the practical solution to this problem is using optical heterodyning.

For example, switching the laser beam frequency can be achieved through acousto-optic modulators [27]. The dual laser beams are combined with a beam splitter (BS) and projected by the x-y scanner towards a 3D object at a distance $z + z_0$ from the back focal plane of the L1 lens. We set the object in a spatial light modulator. An amplitude transmittance T(x,y,z) represents each slice of the object.

The SLM displays the brain tumor image, I(x,y,z), located at a distance $z + z_0$ away from the back focal plane of the lens L1, Furthermore, the first attempts to develop SLMs suffer from a diffraction efficiency problem arising from phase shift loss. In this case, as the MRI image is a binary image, the SLM used can achieve an offset range approaching 2π, which results in excellent diffraction efficiency. Besides, the SLM is a recent device allowing modulating the blazing functions to achieve maximum grating efficiency and high diffraction performance.

We place the object in front of the lens L_2 of the Fourier transform. The amplitude distributions of the two laser beams before the object slice at the $z + z_0$ position is mathematically given by:

$$\begin{aligned} &P(x, y, z + z_0) \\ &= P^1_{z+z_0}\left(\frac{k_0 x}{f}, \frac{k_0 y}{f}\right) e^{j\omega t} \\ &+ P^2_{z+z_0}\left(\frac{k_0 x}{f}, \frac{k_0 y}{f}\right) e^{j(\omega+\psi)t}, \end{aligned} \tag{1}$$

where

$$P^{i}_{z+z_0}\left(\frac{k_0 x}{f},\frac{k_0 y}{f}\right) = P^{i}\left(\frac{k_0 x}{f},\frac{k_0 y}{f}\right) * h(x,y,z+z_0) = F\{P^{i}(x,y)\}_{k_x,k_y} * h(x,y,z+z_0) \quad (2)$$

with i =1,2 and

$$F\{P^{i}(x,y)\}_{k_x,k_y} = \iint_{-\infty}^{+\infty} P^{i}(x,y) e^{j(k_x x + k_y y)} dxdy \quad (3)$$

Equation 3 is the Fourier transform of P_i (x, y), where in k_x and k_y designate the spatial frequencies associated with the variables x and y, accordingly, in equation 1.

$$h(x,y,z+z_0) = e^{-jk_0(z+z_0)} \frac{jk_0}{2\pi(z+z_0)} e^{\frac{-jk_0}{2(z+z_0)}(x^2+y^2)} \quad (4)$$

Equation 4 is the free space spatial impulse response in Fourier optics [20], where in k_0 is the wave number of the laser beam; the field right after the object is:

$$i_\psi(t) = Re\left(\int \left[P^{2}_{z+z'}(x',y') T(x'+x,y'+y,z')\,dx'\right] \times \int \left[P^{1\,*}_{z+z'}(x',y')\, T^{*}(x''+x,y''+y,z'')\,dx''\,dy''\,dz''\right] e^{j\psi t}\right), \quad (5)$$

where x = x(t) and y = y(t) representing the current 2D Position of the object in terms of the distribution of the light amplitude. This field propagates across the lens L2 of the Fourier transform and reaches the mask, M(x, y), located in the back focal plane of the lens L_2. The distribution of the field coming out of the mask, from all slices of the object T(x, y, z), is as follows:

$$A(x,y;x_M,y_M) \propto \left\{P^{1}_{z+z_0}(x',y') e^{j\omega t} + P^{2}_{z+z_0}(x',y') e^{j(\omega+\psi)t}\right\} T(x'+x,y'+y,z') \times \left\{\exp\left(\frac{jk_0}{f}(x' x_M + y' y_M)\right)\,dx'\right\} \left\{\exp\left(-\frac{jk_0 z}{2f}({x_M}^2 + {y_M}^2)\right)\,dz\right\}, \quad (6)$$

where x_M and y_M are the coordinates in the mask plane, and z is the distance to the slice of the object that is located at SLM, measured from the front focal plane of the lens L_2. Following the integration on z represents the volumetric e_ect due to the 3D object. Finally, the photodetector (PD), which is sensitive to the intensity, yields the output current i(t) through spatial integration of the intensity:

$$i(t) \propto \int |A(x,y;x_M,y_M)|^2 dx_M dy_M \quad (7)$$

i(t) is composed of a base-band current and a heterodyne current at the frequency ψ. After several manipulations, the current heterodyne i(t), coming out of the bandpass filter (see Fig. 1), is yielded by [23]:

$$i_{\psi_Q}(x,y,z+z_0) = P^{1}_{z+z_0}\left(\frac{k_0 x'}{f},\frac{k_0 y'}{f}\right) P^{2\,*}_{z+z_0}\left(\frac{k_0 x'}{f},\frac{k_0 y'}{f}\right) \otimes |O(x,y,z+z_0)|^2 \quad (8)$$

Afterward, we are able to define the optical transfer function (OTF) of the system by:

$$OTF_\psi(k_x,k_y,z+z_0) = \frac{F\left\{i_{\psi_Q}(x,y,z+z_0)\right\}}{F\{|O(x,y,z+z_0)|^2\}} \quad (9)$$

As a result, we obtain the following equations:

$$\mathrm{i_c(x,y)} = \mathrm{Re}\left\{\int \mathrm{F^{-1}\{F\{|O(x,y,z+z_0)|^2\}.OTF_\Psi\}\,dz}\right\} \quad (10)$$

$$\mathrm{i_s(x,y)} = \mathrm{Im}\left\{\int \mathrm{F^{-1}\{F\{|O(x,y,z+z_0)|^2\}.OTF_\Psi\}\,dz}\right\} \quad (11)$$

These two currents are respectively representing the In-phase component i_c (x, y) and the quadrature component i_s (x, y) of the extracted heterodyne current from the scanned MR image. the temporal frequency shift is inserted between the two pupils by assuming P^{1}_{z+z0} (x, y) = 1 and P^{2}_{z+z0}(x, y) =δ(x, y) Thus, the optical transfer function becomes:

$$\mathrm{OTF_\Psi(k_x,k_y,z+z_0)} = \exp\left[\frac{-\mathrm{j(z+z_0)}}{2\mathrm{k_0}}(\mathrm{k_x}^2 + \mathrm{k_y}^2)\right] \quad (12)$$

and the two streams become:

$$\mathrm{i_c(x,y)} = \int \left\{|\mathrm{O(x,y,z+z_0)}|^2 * \frac{\mathrm{k_0}}{2\pi(\mathrm{z+z_0})} \sin\left[\frac{\mathrm{k_0}}{2(\mathrm{z+z_0})}(\mathrm{x^2+y^2})\right]\right\} \mathrm{dz} \quad (13)$$

$$i_s(x,y) = \int \left\{|O(x,y,z+z_0)|^2 * \frac{k_0}{2\pi(z+z_0)} cos\left[\frac{k_0}{2(z+z_0)}(x^2+y^2)\right]\right\} dz \quad (14)$$

The proposed approach's basic idea is to use the In-phase component $i_c(x,y)$ for detecting abnormal tissue in MR images. The optical system in Fig. 1 gives an output that shows the distribution of the In-phase component of the heterodyne current. Maximum values characterize this output called the In-phase component peaks. Fig. 2 shows examples of the In-phase component peaks given by the GOSH method.

Therefore, determining the brain tumor's position by searching the peaks given by the maximum values of the In-phase component distribution. With the peaks position of the In-phase component, as shown in Fig. 3, we extract the initial contour C_i of the tumor segmentation within the tumor tissue. The proposed method can be adapted to detect multimodal tumors by detecting the two maxima's two positions of the In-phase component peaks.

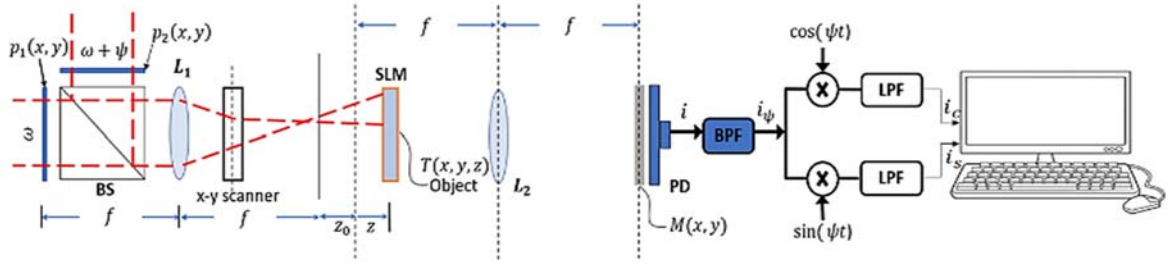

Fig. 1. Generalized two-pupil heterodyne scanning image processing system for the In-phase component extraction of brain tumor.

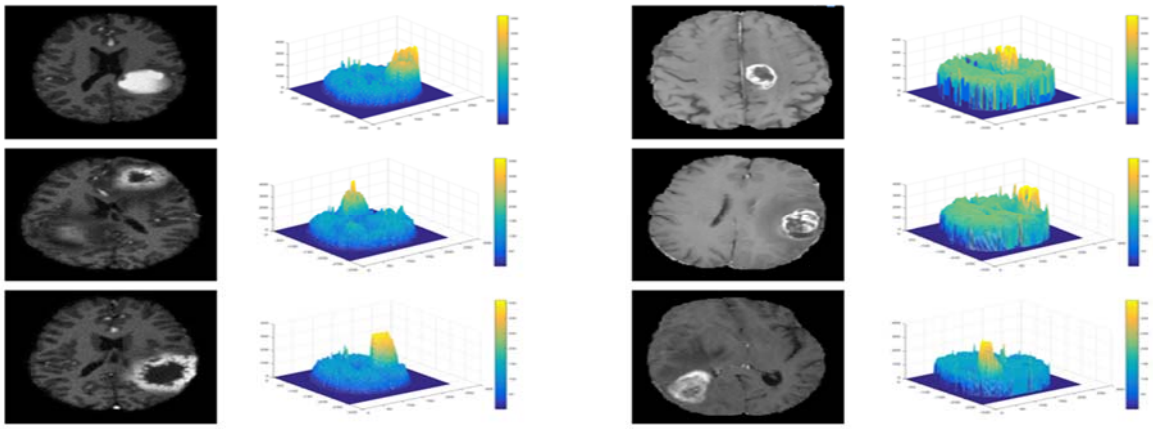

Fig. 2. In-phase component peaks at the tumor position according to the proposed method GOSH: BRATS 2012 and BRATS 2013 database images.

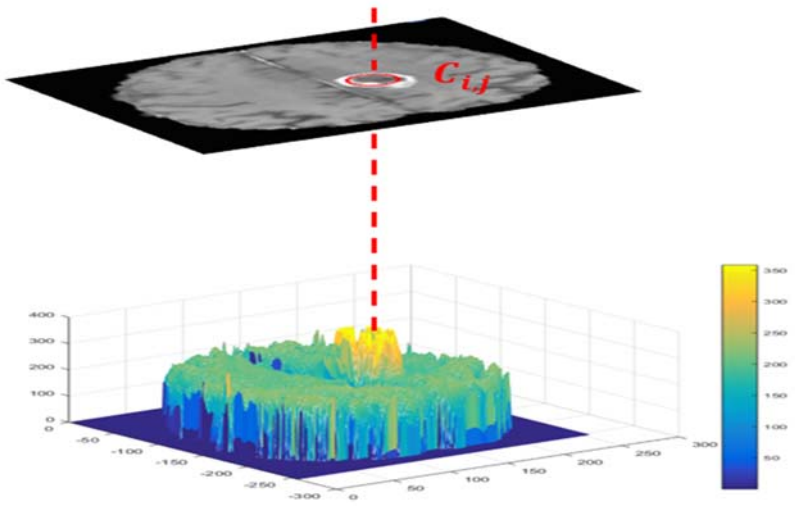

Fig. 3. Principle of extracting the initial contour C_i within the tumor tissue, by GOSH method based on In-phase component peaks.

In a digital system, the OSH optical process results are used for extracting the following parameters: c the center of the tumor, L the amplitude of the In-phase component peak, and C_i the initial contour formed using the principal in Fig. 3. The suggested method detects tumor tissue and facilitates the energy calculation of active contours. Using the initially detected contour C_i, we calculate the averages of the image I (x, y) inside C_i and outside C_i to define the active contour model:

$$E_{i,j} = \alpha . C_{i,j} + \beta . \left| I - M_{i,j} \right|^2 + \gamma . \left| I - m_{i,j} \right|^2, \quad (15)$$

where: $\alpha = \beta = \gamma = 1$ are fixed parameters. $C_{i,j}$ is the initial contour detected by the proposed method. mi,j is the average of the input RM image I(x,y) inside the initial contour $C_{i,j}$. $M_{i,j}$ is the average of the input RM image I(x,y) outside the initial contour $C_{i,j}$. Besides, the evolution of the initial contour detected by the GOSH system is realized through the programming of the proposed active contour pattern, based on finite differences obtained after linearization and discretization of Eq's energy 15. The lecturer can find more details about applying the active contour model proposed in our previous work in[16]. Fig. 4 shows examples of tumor segmentation through the proposed GOSH method.

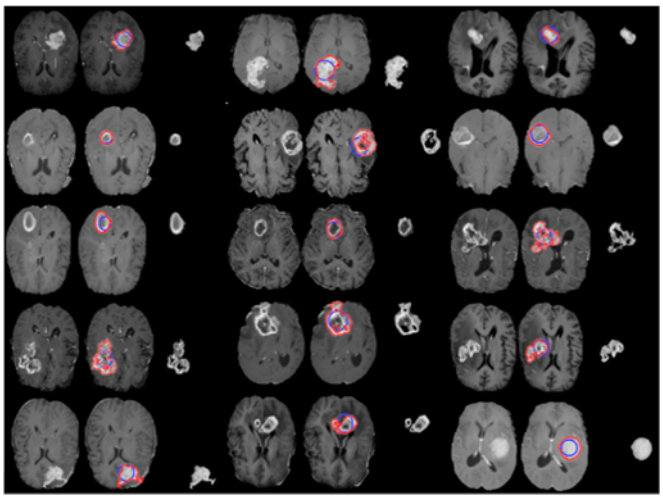

Fig. 4. Segmentation results collected from the BRATS 2012 and 2013 databases. ■ : Initial contours detected through the GOSH method, ■ : Definitive contours after the GOSH method evolution.

3. Experimental Results

In this part, we first evaluate the performance of the proposed method concerning brain tumor detection. For that, we assess the two-parameter returned by the GOSH: the center of tumor c and the maximum peak value of the In-phase component L. Two databases, BRATS 2012 and BRATS 2013 (https://www.smir.ch/BRATS/Start2016), were used for all the tests due to ground truths' availability [28]. In order to evaluate the methods used, four similarity criteria were considered: the Sensitivity Sen, the Dice coefficient D, the Hausdorff distance H_d, and the Specificity Spe calculated as below:

$$0 \le Sen = \frac{TP}{TP + FN} \le 1 \quad (16)$$

$$0 \le D = \frac{TP}{TP + \frac{FP + FN}{2}} \le 1 \quad (17)$$

$$0 \le Sep = \frac{TN}{TN + FP} \le 1, \quad (18)$$

where in TP is the true positive (pixels correctly classified as a tumor tissue), TN is the true negative (pixels correctly classified as healthy tissue), FP is the false positive (normal tissue incorrectly classified as tumor region), and FN is the false negative (undetected tumor tissue).

$$H_d(G,S) = \max\left\{\max_{a \in G} \min_{b \in S} \|a - b\|, \max_{b \in S} \min_{a \in G} \|b - a\|\right\}, \quad (19)$$

where G is the ground truth or gold standard and S is the automatically obtained result. The perfect correspondence is obtained when the metrics Sen, D, and Spe are equal to 1 and the ideal value of H_d(G, S) is 0.

3.1. Brain Tumor Detection

Research in the area of dosimetry planning and radiotherapy is progressing at a staggering pace. Since the first surveys, it has been widely used to inject a curative and precise dose of radiation, mainly through automatic detection and segmentation methods. Such methods are unfortunately limited in real life as they suffer a lack of full automaticity in terms of tumor detection. Our method solved this limitation by using

the maximum peaks of In-phase components extracted by the GOSH process.

As the decision of the existence of a brain tumor on an MR image is based on the parameter L, we have studied L values for MR images of healthy and tumor brains. Fig. 5 represents the statistical distribution of the L parameter in the two cases mentioned. Evidently, in the case of the tumor, L values are large compared to the healthy brain. In the images of healthy brains, the average L in the images used was 110, and in the images of brain tumors was 325. It should be noted that the maximum peaks of In-phase components given by the GOSH process, which localized the tumors, were within the margin of [300; 350]. This margin increases to over 255 due to the multiplication of the MRI images in equation 10. Moreover, due to the uniform distribution of pixel intensity in images of the healthy brain, all of the maximum peaks of the In-phase component in cases of healthy brains being within [100 120]. Therefore, the parameter L given by the GOSH process is a reliable parameter to decide the existence of a tumor in the MR images.

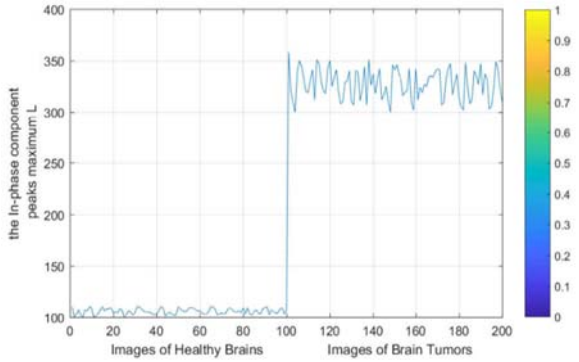

Fig. 5. Distribution of the L parameter in the healthy and tumorous brain images.

Similarly, the brain tumor position's decision is based on the parameter c given by the GOSH. Therefore, we have estimated the precision of the proposed method regarding the detection of c inside of the tumor tissue. As a comparison, we have also calculated the percentage rate of the potential field segmentation (PFS) algorithm [29] regarding tumor centers' detection. This approach is founded on potential field analogy in detecting brain tumors by assuming the intensity of a pixel as a mass, creating a potential field.

It should be pointed out that the center used is obtained from the maximum peaks of the In-phase component. Table 1 reveals the high accuracy of detecting the center of the tumor tissue by the proposed method. In 98.5% of the patients (from both databases), the maximum peaks of In-phase components given by the proposed method are located in the tumor tissue center. In the remaining 1.5%, the GOSH returned parameter c to the border of this tumor. Two principal reasons explain these results; firstly, owing to the modalities used in MR images to separate tumors from healthier tissue, contrast provides an almost unique signature for each type of tissue, particularly the type of tumor, which appears in most cases with the white color. Secondly, the high value of the maximum peaks of the In-phase component in tumoral regions. Therefore, the proposed method is a promising technique for detecting anomalous tissue in MR images, comparing with recently published methods. The proposed method is more accurate and quicker. It should be noted that the center used is determined by the maximum peak of the In-phase component.

Table 1. Percentage of the proposed method in terms of the c parameter return within the tumor tissue and the meantime, comparing to the method of [29].

Method	Accuracy (%)			Time average (s)
	Inside tumor	Edge tumor	Outside tumor	
Potential Field [29]	95 %	0	5 %	38.1643
Proposed method	98.5 %	1.5 %	0%	0.2009

3.2. Brain Tumor Segmentation

Once the GOSH technique has automatically and quickly detected the tumor tissue, we can discuss OSH's advantages in part devoted to segmentation. For this purpose, we have investigated several active contour models (ACM) based on the GOSH. All the ACM processes have been initialized with the proposed GOSH's initial contours for relevant comparison.

To test the proposed method in a very demanding way and link it to clinical imaging applications, we have used 20 images of patients with the most challenging segmentation conditions. These images contain different shapes, sizes, and contrasts of tumors, Tables 2 - 3 compare the performance reported from these 20 images and reached by the GOSH method with the Geodesic Active Contour model (GAC) [30], the Localized Active Contour (LAC) [31], the Active Contours by Cuckoo Search (ACCS) [32] and our previous work OSH-ACM [1]. Compared to other ACMs, the proposed method performs better in terms of Sen, D, H, and Spe parameters. For evidence, the sensitivity value of 0.9961 reached by the proposed method was the highest obtained, and its Hausdorff distance of 2.0000 was the lowest. Besides, its highest average specificity value of Spe = 1:0000 indicates that it can correctly classify healthy tissue more than other ACM-based methods. It should be noted that the highly efficient performance of all methods in terms of the Spe parameter is explained by

the fact that all the initial contours detected by the proposed GOSH technique are located inside the tumor tissue. Following these methods' development, the optimal segmentation contours remain inside the tumor tissue, making the FP parameter very close to zero. Also, it can be observed from Tables 2 and 3 that the proposed method reduces the calculation time (in seconds).

Table 2. Sensitivity, Dice, Hausdorff distance, Specificity, and elapsed time rates obtained from the optimal contour of the **BRATS 2012** database images reached by using the Geodesic Active Contour (GAC), the Localized Active Contour (LAC), the Active Contour driven by Cuckoo Search (ACCS), our previous work (OSH-ACM) and the proposed method (Proposed).

Patients	Method	Sen	D (AVG±SDx10^{-4})	H_d	Spe	Time (s)
Patient 1 (BRATS 2012)	GAC	0.7194 ±1.2	0.7650±6.3	4.1200 ±2.6	0.9945±0.0	14.9945±1.2
	LAC	0.9016 ±2.6	0.9482±3.3	2.7488 ±2.6	0.9975±2.3	14.2406±1.9
	ACCS	0.9502 ±7.5	0.9495±9.0	2.6488 ±5.2	0.9980±1.0	48.1200±2.0
	OSH-ACM	0.9772 ±0.5	0.9838±0.3	2.0458 ±0.0	0.9987±4.5	0.2937±3.1
	Proposed	**0.9809** ±0.7	**0.9896**±0.1	**2.0402**±0.1	**0.9989**±2.5	**0.2463**±2.1
Patient 2 (BRATS 2012)	GAC	0.7844 ±0.0	0.7377 ±4.2	4.3589 ±6.1	0.9903 ±4.5	26.1737 ±2.5
	LAC	0.8250 ±5.4	0.9041 ±4.8	4.0010 ±2.0	0.9957 ±2.8	17.1943 ±9.5
	ACCS	0.9347 ±1.5	0.9605 ±0.8	3.0050 ±2.5	0.9989 ±1.1	46.9430 ±9.0
	OSH-ACM	0.9752 ±0.2	0.9753 ±0.1	2.1623 ±0.0	0.9980 ±0.0	0.3540 ±7.2
	Proposed	**0.9879** ±0.4	**0.9802** ±0.6	**2.1597** ±0.2	**0.9987** ±0.1	**0.3232** ±8.2
Patient 3 (BRATS 2012)	GAC	0.6804 ±6.3	0.7489 ±5.6	5.7823 ±2.4	0.9902 ±0.3	27.7494 ±2.8
	LAC	0.6715 ±2.3	0.8417 ±5.3	4.8990 ±7.5	0.9914 ±0.0	17.3898 ±7.0
	ACCS	0.9274 ±3.8	0.9410 ±4.1	3.5560 ±7.1	0.9992 ±0.9	59.2705 ±2.7
	OSH-ACM	0.9898 ±0.1	0.9897 ±0.1	2.0623 ±1.0	1.0000 ±0.1	0.2530 ±3.8
	Proposed	**0.9899** ± 0.0	**0.9898 ±0.0**	**2.0596 ±3.0**	**1.0000 ±0.1**	**0.2498 ±2.4**
Patient 4 (BRATS 2012)	GAC	0.5751 ±3.7	0.6456 ±0.1	4.1231 ±8.7	0.9976 ±1.7	37.9528 ±8.7
	LAC	0.6346 ±2.0	0.7765 ±1.0	4.3589 ±5.7	0.9950 ±4.6	17.6072 ±8.0
	ACCS	0.8892 ±3.9	0.9395 ±1.0	3.3940 ±3.3	0.9989 ±7.4	25.7492 ±5.4
	OSH-ACM	0.9867 ±0.1	0.9834 ±0.1	2.0056 ±1.0	0.9997 ±0.7	0.2212 ±1.5
	Proposed	**0.9884 ±0.0**	**0.9905 ±0.6**	**2.0024 ±5.0**	**0.9999 ±0.2**	**0.2200 ±1.0**
Patient 5 (BRATS 2012)	GAC	0.7247 ±3.4	0.6902 ±2.8	5.7958 ±3.9	0.9906 ±5.5	22.1867 ±9.6
	LAC	0.7678 ±2.0	0.7243 ±0.0	4.0001 ±1.0	0.9907 ±0.5	16.6965 ±0.8
	ACCS	0.9192 ±2.1	0.9380 ±0.2	3.5437 ±1.0	0.9984 ±6.6	18.4792 ±0.8
	OSH-ACM	0.9894 ±0.2	0.9757 ±0.1	2.5826 ±1.0	0.9997 ±4.4	0.2165 ±2.6
	Proposed	**0.9899 ±0.1**	**0.9864 ±0.2**	**2.459 ±3.0**	**0.9997 ±0.3**	**0.2130 ±0.6**
Patient 6 (BRATS 2012)	GAC	0.7800 ±5.4	0.8096 ±1.7	3.0010 ±2.0	0.9950 ±2.2	9.3899 ±7.4
	LAC	0.7473 ±0.3	0.7181 ±0.1	3.0000 ±0.0	0.9975 ±7.9	10.5313 ±0.9
	ACCS	0.9247 ±2.0	0.9400 ±2.3	2.8947 ±9.7	0.9998 ±2.3	15.3692 ±5.0
	OSH-ACM	0.9898 ±1.7	0.9887 ±1.2	2.0620 ±0.0	0.9995 ±3.8	0.1730 ±2.6
	Proposed	**0.9902 ±0.8**	**0.9942 ±5.8**	**2.0329 ±0.5**	**0.9998 ±9.7**	**0.1710 ±4.6**
Patient 7 (BRATS 2012)	GAC	0.5154 ±0.4	0.6069 ±0.4	5.3852 ±0.0	0.9963 ±2.7	26.4020 ±4.0
	LAC	0.6850 ±0.4	0.6436 ±0.2	4.9904 ±0.3	0.9975 ±7.0	14.1543 ±6.6
	ACCS	0.8995 ±1.2	0.9364 ±5.6	2.9634 ±2.3	0.9986 ±0.9	28.3751 ±5.9
	OSH-ACM	0.9789 ±1.5	0.9871 ±1.1	2.0458 ±0.0	0.9997 ±0.0	0.1356 ±1.8
	Proposed	**0.9808 ±5.6**	**0.9894 ±6.2**	**2.0389 ±1.0**	**0.9996 ±0.0**	**0.1310 ±2.9**
Patient 8 (BRATS 2012)	GAC	0.5471 ±0.4	0.5565 ±0.3	5.8990 ±1.0	0.9904 ±0.5	24.9600 ±1.3
	LAC	0.7693 ±0.6	0.7895 ±0.5	4.3852 ±1.0	0.9985 ±2.8	16.8878 ±1.0
	ACCS	0.9599 ±0.6	0.9601 ±4.0	2.7945 ±0.0	0.9950 ±3.3	36.7810 ±1.8
	OSH-ACM	0.9886 ±2.4	0.9749 ±1.0	2.0827 ±1.1	0.9987 ±4.6	0.1321 ±3.6
	Proposed	**0.9888 ±1.4**	**0.9780 ±2.0**	**2.0684 ±2.5**	**0.9996 ±2.4**	**0.1329 ±4.7**
Patient 9 (BRATS 2012)	GAC	0.6878 ±0.2	0.6558 ±0.0	5.0915 ±0.2	0.9967 ±0.0	15.7585 ±4.5
	LAC	0.8095 ±0.0	0.8947 ±0.1	3.1623 ±2.0	0.9974 ±7.7	8.5422 ±8.9
	ACCS	0.9097 ±3.0	0.8997 ±0.4	3.1597 ±5.3	0.9988 ±9.6	17.1467 ±2.4
	OSH-ACM	0.9877 ±1.4	0.9782 ±0.5	2.1284 ±0.0	0.9996 ±0.8	0.1879 ±0.3
	Proposed	**0.9899 ±0.9**	**0.9842 ±0.2**	**2.0084 ±0.2**	**0.9997 ±1.5**	**0.1479 ±1.9**
Patient 10 (BRATS 2012)	GAC	0.5499 ±0.3	0.4998 ±0.1	6.7823 ±0.0	0.9945 ±9.1	20.8182 ±6.2
	LAC	0.6867 ±0.3	0.6577 ±0.1	5.1644 ±0.1	0.9959 ±2.2	8.0357 ±9.8
	ACCS	0.9002 ±4.2	0.9147 ±2.5	2.9846 ±7.3	0.9979 ±0.4	18.7666 ±0.0
	OSH-ACM	0.9868 ±1.0	0.9786 ±0.2	2.0628 ±1.0	0.9997 ±2.0	0.2429 ±4.7
	Proposed	**0.9961 ±6.0**	**0.9882 ±4.2**	**2.0304 ±9.0**	**0.9997 ±0.0**	**0.2099 ±8.2**

Table 3. Sensitivity, Dice, Hausdorff distance, Specificity, and elapsed time rates obtained from the optimal contour of the **BRATS 2013** database images reached by using the Geodesic Active Contour (GAC), the Localized Active Contour (LAC), the Active Contour driven by Cuckoo Search (ACCS), our previous work (OSH-ACM) and the proposed method (Proposed).

Patients	Method	Sen	D (AVG±SDx10^{-4})	H_d	Spe	Times (s)
Patient 11 (BRATS 2013)	GAC	0.7607 ±0.2	0.7185 ±0.0	3.1623 ±0.1	0.9933 ±1.8	12.3015 ±8.9
	LAC	0.8068 ±0.1	0.8931 ±1.8	2.8361 ±0.6	0.9964 ±2.8	8.2133 ±8.7
	ACCS	0.9547 ±0.0	0.9328 ±4.4	2.5138 ±9.7	0.9973 ±0.7	22.8520 ±3.3
	OSH-ACM	0.9876 ±1.5	0.9882 ±0.8	2.1166 ±1.0	0.9987 ±1.0	0.2820 ±4.3
	Proposed	**0.9896 ±0.0**	**0.9893 ±0.2**	**2.1040 ±0.0**	**0.9989 ±0.0**	**0.2095 ±7.2**
Patient 12 (BRATS 2013)	GAC	0.6573 ±0.4	0.6718 ±0.5	6.4721 ±2.0	0.9934 ±6.3	37.0503 ±5.1
	LAC	0.7185 ±4.0	0.7832 ±0.3	3.7417 ±0.0	0.9967 ±4.9	6.2981 ±8.1
	ACCS	0.9009 ±3.7	0.9343 ±2.4	2.9987 ±0.0	0.9972 ±0.4	19.7351 ±0.8
	OSH-ACM	0.9898 ± 0.1	0.9847 ±0.0	2.0495 ±0.0	0.9989 ±5.5	0.1013 ±1.5
	Proposed	**0.9900 ±9.0**	**0.9904 ±5.2**	**2.0398 ±5.0**	**0.9997 ±4.2**	**0.1010 ±2.9**
Patient 13 (BRATS 2013)	GAC	0.5080 ±0.3	0.5443 ±0.2	5.7446 ±0.5	0.9930 ±2.0	36.8782 ±4.7
	LAC	0.6304 ±0.5	0.6307 ±0.4	4.4721 ±0.0	0.9911 ±0.9	8.6424 ±1.3
	ACCS	0.8975 ±0.7	0.9051 ±6.6	3.3001 ±3.3	0.9970 ±1.0	28.4568 ±9.6
	OSH-ACM	0.9887 ±0.1	0.9865 ±0.1	2.1417 ±1.0	0.9987 ±2.2	0.1468 ±0.2
	Proposed	**0.9890 ±2.0**	**0.9894 ±1.2**	**2.1314 ±9.0**	**0.9996 ±3.1**	**0.1316 ±8.1**
Patient 14 (BRATS 2013)	GAC	0.7040 ±0.3	0.7755 ±0.7	3.4495 ±0.0	0.9900 ±3.2	10.4806 ±6.4
	LAC	0.8897 ±0.1	0.8825 ±0.0	3.1200 ±1.12	0.9956 ±7.9	3.9965 ±8.0
	ACCS	0.9110 ±3.3	0.8997 ±2.2	3.2546 ±6.9	0.9967 ±0.7	44.3490 ±3.7
	OSH-ACM	0.9769 ±1.4	0.9769 ±1.2	2.0000 ±0.0	0.9987 ±2.3	0.2164 ±1.3
	Proposed	**0.9802 ±5.6**	**0.9890 ±3.2**	**2.0000 ±0.0**	**0.9996 ±8.4**	**0.2030 ±5.2**
Patient 15 (BRATS 2013)	GAC	0.6699 ±0.3	0.5401 ±0.0	4.2426 ±0.5	0.9963 ±2.7	20.9238 ±7.3
	LAC	0.6436 ±0.1	0.7043 ±0.0	3.4641 ±0.0	0.9977 ±2.7	3.4695 ±0.2
	ACCS	0.9567 ±0.0	0.9476 ±1.2	2.7640 ±2.8	0.9976 ±2.4	30.2648 ±4.5
	OSH-ACM	0.9887 ±0.1	0.9887 ±1.0	2.0458 ±1.1	0.9997 ±0.0	0.1357 ±0.7
	Proposed	**0.9899 ±2.5**	**0.9904 ±9.0**	**2.0053 ±9.1**	**0.9997 ±0.0**	**0.1300 ±0.9**
Patient 16 (BRATS 2013)	GAC	0.6917 ±0.4	0.6517 ±0.2	5.6569 ±5.5	0.9955 ±4.8	36.9248 ±7.2
	LAC	0.8937 ±0.1	0.8850 ±0.0	3.6904 ±1.0	0.9971 ±3.8	6.0861 ±8.3
	ACCS	0.9379 ±9.8	0.9471 ±2.7	2.8000 ±0.0	0.9989 ±4.4	34.7982 ±0.8
	OSH-ACM	0.9886 ±0.2	0.9891 ±0.1	2.1056 ±1.0	0.9990 ±0.0	0.2294 ±3.8
	Proposed	**0.9902 ±8.1**	**0.9900 ±5.2**	**2.1009 ±9.0**	**0.9996 ±0.0**	**0.2064 ±5.2**
Patient 17 (BRATS 2013)	GAC	0.5269 ±0.4	0.5252 ±0.3	6.4807 ±0.0	0.9945 ±1.4	38.9236 ±8.6
	LAC	0.6864 ±0.4	0.7052 ±0.3	3.7417 ±0.0	0.9958 ±2.2	13.6119 ±0.8
	ACCS	0.9007 ±2.1	0.9111 ±2.8	3.5781 ±5.5	0.9973 ±2.2	34.2876 ±2.2
	OSH-ACM	0.9839 ±0.1	0.9712 ±0.0	2.1024 ±1.0	0.9987 ±0.7	0.2165 ±2.4
	Proposed	**0.9902 ±4.2**	**0.9890 ±0.8**	**2.1000 ±3.0**	**0.9997 ±1.9**	**0.1990 ±8.7**
Patient 18 (BRATS 2013)	GAC	0.5748 ±2.3	0.5180 ±7.5	6.7727 ±2.0	0.9910 ±4.5	44.1824 ±5.9
	LAC	0.8753 ±0.0	0.8935 ±1.7	3.9990 ±0.1	0.9928 ±6.3	15.1849 ±7.4
	ACCS	0.9018 ±3.7	0.9124 ±8.6	3.3179 ±2.4	0.9979 ±5.8	38.7530 ±0.2
	OSH-ACM	0.9850 ±0.1	0.9760 ±0.0	2.0361 ±0.0	0.9987 ±2.4	0.1834 ±0.5
	Proposed	**0.9902 ±4.2**	**0.9801 ±2.0**	**2.0254 ±0.0**	**0.9996 ±2.0**	**0.1664 ±0.1**
Patient 19 (BRATS 2013)	GAC	0.7629 ±0.0	0.7655 ±0.1	3.2361 ±1.0	0.9986 ±6.7	20.4650 ±0.4
	LAC	0.7279 ±0.2	0.6910 ±0.0	4.8759 ±0.2	0.9984 ±0.8	6.3258 ±8.4
	ACCS	0.8974 ±4.7	0.9046 ±2.7	3.7000 ±0.0	0.9990 ±0.2	33.4758 ±0.4
	OSH-ACM	0.9815 ±1.3	0.9720 ±0.4	2.0730 ±1.0	1.0000 ±0.0	0.2100 ±0.0
	Proposed	**0.9900 ±8.0**	**0.9924 ±8.1**	**2.0345 ±5.0**	**1.0000 ±0.0**	**0.1600 ±0.0**
Patient 20 (BRATS 2013)	GAC	0.8193 ±0.0	0.9007 ±0.0	3.6458 ±1.0	0.9980 ±3.4	11.2779 ±4.9
	LAC	0.8467 ±0.0	0.9170 ±0.0	3.0458 ±1.6	0.9985 ±9.7	3.2656 ±5.3
	ACCS	0.9544 ±2.4	0.9590 ±2.4	3.0001 ±9.7	0.9995 ±2.4	27.2486 ±0.4
	OSH-ACM	0.9779 ±1.0	0.9823 ±0.4	2.0475 ±0.2	0.9997 ±3.1	0.1547 ±3.2
	Proposed	**0.9800 ±2.0**	**0.989192 ±8.2**	**2.0362 ±4.1**	**0.9997 ±0.0**	**0.1377 ±8.2**

The proposed GOSH method detects the initial contour inside the tumor in real-time, making it possible to calculate the time required for the active contour to evolve. Therefore, the proposed method is the quickest approach. Overall, the proposed GOSH-AC method is a technique for automatic detection and fast segmentation of brain tumors. It solves the manual segmentation of tumors performed by experts and

error-prone, sensitive, and time-absorbing process. The GOSH process is a fully automatic process offering an accuracy of 100 % in detecting all tumor types. Besides, its returned parameter L is a trustworthy parameter for deciding the MR images tumor position. Moreover, the proposed method is more efficient in terms of segmentation.

4. Conclusions

In this paper, we enhance our previous research [1, 33] in terms of acquisition speed, precision, and data size. The proposed method detects the brain tumor's position using two parameters (L, c) returned by the GOSH technique. The underlying physics behind the obtained results (Tables 2 and 3) is the fast computation of the extraction of In-phase components' peaks maximums in the MR image. Besides, this approach's main advantage is the short computation time, the automaticity, and the reliable precision of segmentation. Hence, we have reached a principal aim to move the active contour theory from semi-automatic to automatic status by the reliable detection of Brain tumors by the Generalized Optical Scanning Holography (GOSH).

Acknowledgements

The authors would like to express thankfulness to Professor Ivan Cabria, Departamento de FsicaTerica, Universidad de Valladolid, Valladolid, Spain, for the details about the source code of his work on the Potential Field Segmentation algorithm. Further, the Authors thank Raphael Meier, Medical Image Analysis Institute for Surgical Technology and Biomechanics, University of Bern, Switzerland, for providing access to the BRATS database.

References

[1]. Abdelaziz Essadike, Elhoussaine Ouabida, and Abdenbi Bouzid, Optical scanning holography for tumor extraction from brain magnetic resonance images, *Optics & Laser Technology*, 127, 2020, 106158.

[2]. Shuaifeng Dou, Xueju Shen, Bing Zhou, Long Wang, and Chao Lin, Experimental research on optical image encryption system based on joint Fresnel transform correlator, *Optics & Laser Technology*, 112, 2019, pp. 56-64.

[3]. Elhoussaine Ouabida, Abdelaziz Essadike, and Abdenbi Bouzid, Automated segmentation of ophthalmological images by an optical based approach for early detection of eye tumor growing, *Physica Medica*, 48, 2018, 37-46.

[4]. Jyotismita Chaki, Brain Tumor MRI Image Segmentation Using Deep Learning Techniques. *Elsevier*, 2021.

[5]. Elhoussaine Ouabida, Abdelaziz Essadike, and Abdenbi Bouzid, Optical approach for iris segmentation and tracking, in *Proceedings of the 4th IEEE International Colloquium on Information Science and Technology (CiSt)*, 2016, pp. 476-480.

[6]. Vijayan K. Asari and M. Nazrul Islam, Special issue on optical image processing, *Optics Laser Technology*, 57, 2014, pp. 227-229.

[7]. Joseph E. Bugaj, Samuel I Achilefu, Richard B. Dorshow, and Raghavan Rajagopalan, Novel uorescent contrast agents for optical imaging of in vivo tumors based on a receptor-targeted dye-peptide conjugate platform, *Journal of Biomedical Optics*, 6, 2, 2001, pp. 122-133.

[8]. Peter Stanley Jørgensen, Karin Vels Hansen, Rasmus Larsen, and Jacob R. Bowen, A framework for automatic segmentation in three dimensions of microstructural tomography data, *Ultramicroscopy*, 110, 3, 2010, pp. 216-228.

[9]. Xiongyao Wang, R. Lockwood, M. Malac, H. Furukawa, P. Li, and A. Meldrum, Reconstruction and visualization of nanoparticle composites by transmission electron tomography, *Ultramicroscopy*, 113, 2012, pp. 96-105.

[10]. J Amorim, B Mendes, E Ribau, M Gouvêa, and S Sarmento, Image processing as a potential tool for CT dose optimization, *Physica Medica*, 32, 2016, 316.

[11]. Diego Roldán, Claudia Redenbach, Katja Schladitz, Matthias Klingele, and Michael Godehardt. Reconstructing porous structures from _b-sem image data: Optimizing sampling scheme and image processing, *Ultramicroscopy*, 226, 2021, 113291.

[12]. Yasuo Kawata, Hidetaka Arimura, Koujirou Ikushima, Ze Jin, Kento Morita, Chiaki Tokunaga, Hidetake Yabu-Uchi, Yoshiyuki Shioyama, Tomonari Sasaki, Hiroshi Honda, et al., Impact of pixel-based machine-learning techniques on automated frameworks for delineation of gross tumor volume regions for stereotactic body radiation therapy, *Physica Medica*, 42, 2017, pp. 141-149.

[13]. Mohamed Aymen Mahjoub, Guillaume Monier, Luc Bideux, Bernard Gruzza, and Christine Robert-Goumet, Multi-mode elastic peak electron microscopy (mm-epem): A new imaging technique with an ultimate in-depth resolution for surface analysis, *Ultramicroscopy*, 188, 2018, pp. 13-18.

[14]. Binlin Wu, Mohammad Alrubaiee, and S. K. Gayen, Time reversal optical tomography: Detecting and locating tumors in an ex vivo model human breast, *Optics & Laser Technology*, 77, 2016, pp. 229-235.

[15]. Zailiang Chen, Dabao Li, Hailan Shen, Hailan Mo, Ziyang Zeng, and Hao Wei, Automated segmentation of uid regions in optical coherence tomography b-scan images of age-related macular degeneration, *Optics & Laser Technology*, 122, 2020, 105830.

[16]. Abdelaziz Essadike, Elhoussaine Ouabida, and Abdenbi Bouzid, Brain tumor segmentation with vander lugt correlator based active contour, *Computer methods and programs in biomedicine*, 160, 2018, pp. 103-117.

[17]. Ting-Chung Poon. Scanning holography and two-dimensional image processing by acoustooptic two-pupil synthesis, *JOSA A*, 2, 4, 1985, pp. 521-527.

[18]. Ting-Chung Poon, Ming Hsien Wu, Kazunori Shinoda, and Yoshiji Suzuki, *Optical scanning holography. Proceedings of the IEEE*, 84, 5, 1996, pp. 753-764.

[19]. Ting-Chung Poon, Richard Juday, and Tsutoma Hara, Spatial light modulatorsresearch, development, and applications: introduction to the feature issue, *Applied Optics*, 37, 32, 1998, pp. 7471-7471.

[20]. T.-C. Poon and Partha P. Banerjee, Contemporary optical image processing with MATLAB, *Elsevier*, 2001.
[21]. Ichirou Yamaguchi, Phase-shifting digital holography. In Digital Holography and Three- Dimensional Display, *Springer*, 2006, pp. 145-171.
[22]. Ting-Chung Poon, Optical scanning holography-a review of recent progress, *Journal of the Optical Society of Korea,* 13, 4, 2009, pp. 406-415.
[23]. Ting-Chung Poon and Guy Indebetouw, Three-dimensional point spread functions of an optical heterodyne scanning image processor, *Applied Optics*, 42, 8, 2003, pp. 1485-1492.
[24]. Ting-Chung Poon. Recent progress in optical scanning holography, *Journal of Holography and Speckle*, 1, 1, 2004, pp. 6-25.
[25]. Ting-Chung Poon, Optical scanning holography with MATLAB, Volume 21, *Springer*, 2007.
[26]. Ting-Chung Poon, On the fundamentals of optical scanning holography, *American Journal of Physics*, 76, 8, 2008, pp. 738-745.
[27]. A Korpel. Acousto-optics, *Marcel Dekker Inc*. New York, 1988.
[28]. Michael Kistler, Serena Bonaretti, Marcel Pfahrer, Roman Niklaus, and Philippe Bûchler, The virtual skeleton database: an open access repository for biomedical research and collaboration, *Journal of Medical Internet Research*, 15, 11, 2013, e245.
[29]. Iván Cabria and Iker Gondra, Mri segmentation fusion for brain tumor detection, *Information Fusion*, 36, 2017, pp. 1-9.
[30]. Vicent Caselles, Ron Kimmel, and Guillermo Sapiro, Geodesic active contours, *International Journal of Computer Vision,* 22, 1, 1997, pp. 61-79.
[31]. Elisee Ilunga-Mbuyamba, Juan Gabriel Avina-Cervantes, Arturo Garcia-Perez, Rene de Jesus Romero-Troncoso, Hugo Aguirre-Ramos, Ivan Cruz-Aceves, and Claire Chalopin, Localized active contour model with background intensity compensation applied on automatic MR brain tumor segmentation, *Neurocomputing*, 220, 2017, pp. 84-97.
[32]. Elisee Ilunga-Mbuyamba, Jorge Mario Cruz-Duarte, Juan Gabriel Avina-Cervantes, Carlos Rodrigo Correa-Cely, Dirk Lindner, and Claire Chalopin, Active contours driven by cuckoo search strategy for brain tumour images segmentation, *Expert Systems with Applications*, 56, 2016, pp. 59-68.
[33]. Anass Cherkaoui, Abdennacer El-Ouarzadi, Abdenbi Bouzid, Younes Achaoui, and Abdelaziz Essadike, Brain Tumor Segmentation by Generalized Optical Scanning Holography (GOSH) Based Active Contour (AC), in *Proceedings of the 6th International Conference on Optics, Photonics and Lasers (OPAL' 2023),* 2023, pp. 44-52.